Research Square

Preprints are preliminary reports that have not undergone peer review.
They should not be considered conclusive, used to inform clinical practice,
or referenced by the media as validated information.

Brainstem–Cerebellar Circuit Dysfunction and Structure–Function Decoupling in Body-First Parkinson's Disease

Lifang She
Nanjing Brain Hospital
Qianxiao Li
Nanjing University
Yunyong Xie
Nanjing University
Sihao Liao
Wuhan University
Guoxiong He
Wuhan University
Hao Wang
Wuhan University
Wei Yu
Wuhan University
Shanshan Feng
Wuhan University
Lina Wang
Huaian First People's Hospital
Xiaoyang Zhang
Nanjing University
Jingning Zhu
Nanjing University
Yang Pan
panyang.zn@whu.edu.cn

Nanjing Brain Hospital

Article

Keywords: Parkinson's disease, Body-first subtype, Dorsal motor nucleus of the vagus, Cerebellum, Resting-state fMRI

Posted Date: November 9th, 2026

DOI: https://doi.org/10.21203/rs.3.rs-11365494/v1

License: This work is licensed under a Creative Commons Attribution 4.0 International License.
Read Full License

Additional Declarations: No competing interests reported.

Brainstem–Cerebellar Circuit Dysfunction and Structure–Function Decoupling in Body-First Parkinson's Disease

Lifang She[1, 7], Qianxiao Li[3, 7], Yunyong Xie[3], Sihao Liao[4], Guoxiong He[4], Liuchen Zhou[4], Hao Wang[4], Shanshan Feng[4], Wei Yu[5], Lina Wang[6], Xiaoyang Zhang[3, *], Jingning Zhu[3, *], Yang Pan[1, 2, *]

[1]Department of Geriatric Neurology, Affiliated Nanjing Brain Hospital of Nanjing Medical University, Nanjing 210029, China.

[2]Department of Neurology, Zhongnan Hospital of Wuhan University, Hubei 430071, China.

[3]State Key Laboratory of Pharmaceutical Biotechnology, National Resource Center for Mutant Mice, Department of Anesthesiology, Nanjing Drum Tower Hospital, Institute for Brain Sciences, and Department of Physiology, School of Life Sciences, Nanjing University, Nanjing 210023, China.

[4]School of Computer Science, Wuhan University, Hubei 430072, China.

[5]School of Artificial Intelligence, Wuhan University, Hubei 430072, China.

[6]Department of Neurology, The Affiliated Huai'an No. 1 People's Hospital of Nanjing Medical University, Huai'an 223300, China.

[7]These authors contributed equally: Lifang She and Qianxiao Li.

[*]These authors are co-corresponding authors.

Correspondence:

Yang Pan, MD

[1]Department of Geriatric Neurology, Affiliated Nanjing Brain Hospital of Nanjing Medical University;

[2]Department of Neurology, Zhongnan Hospital of Wuhan University

Address: Department of Neurology, Zhongnan Hospital of Wuhan University, No. 169, Donghu Road, Wuhan 430071, Hubei, China.

Email: panyang.zn@whu.edu.cn

Tel: +86-18672966786

Co-corresponding authors:

Xiaoyang Zhang, PhD (Email: xiaoyangzhang@nju.edu.cn)

Jingning Zhu, PhD (Email: jnzhu@nju.edu.cn)

Abstract

Parkinson's disease (PD) is heterogeneous, but imaging features of body-first PD remain incompletely characterized. In this case-control study, 54 patients were classified by probable rapid eye movement sleep behavior disorder timing relative to motor onset as body-first (n = 24) or brain-first PD (n = 30), alongside 30 healthy controls. Multimodal MRI assessed dorsal motor nucleus of the vagus (DMV)-seeded functional connectivity, local activity, regional homogeneity, cerebellar gray matter volume, and structure–function decoupling. Body-first PD showed increased DMV–cerebellar connectivity, with convergent abnormalities in bilateral lobule VIII comprising increased activity and synchrony, lower gray matter volume, and greater structure–function mismatch. Higher DMV–lobule VIII connectivity was associated with worse gait, motor, non-motor, and sleep burden after covariate adjustment. Normative Allen Human Brain Atlas analysis identified developmental and signal-regulatory enrichment. These findings suggest a DMV–lobule VIII imaging phenotype associated with clinically defined body-first PD.

Keywords: Parkinson's disease; Body-first subtype; Dorsal motor nucleus of the vagus; Cerebellum; Resting-state fMRI

Introduction

Parkinson's disease (PD) is among the fastest-growing neurodegenerative disorders worldwide [1,2], and is neuropathologically defined by the misfolding and aggregation of α-synuclein, leading to the progressive neuronal degeneration [3,4]. Accumulating neuropathological and imaging evidence has motivated a body-first/brain-first framework in which PD may follow distinct patterns of disease initiation and propagation [5-7]. In the brain-first phenotype, pathology is hypothesized to arise predominantly within the central nervous system [8-10], whereas the body-first phenotype is proposed to involve early peripheral or autonomic structures with subsequent rostral propagation. In these patients, non-motor symptoms precede motor onset [11,12], most notably rapid eye movement sleep behavior disorder (RBD) [13,14], which has emerged as an important clinical indicator of the body-first trajectory [3,15-18], and a clinical proxy for subtype assignment [19].

The dorsal motor nucleus of the vagus (DMV) is a critical relay within the gut-brain axis and an early site of Lewy pathology [20-23]. Experimental and review evidence indicates that peripheral α-synuclein pathology can spread to the DMV after gastrointestinal inoculation [24-28], accompanied by progressive loss of cholinergic neurons [29,30]. These findings position the DMV as a putative gateway for peripheral-to-central α-synuclein propagation, particularly in body-first PD [31]. However, whether and how DMV-centered neural circuits differ between body-first and brain-first subtypes remains largely unexplored.

Here, we employed rs-fMRI and multimodal cerebellar analyses to characterize

DMV-centered network alterations in clinically stratified PD patients. By delineating subtype-specific DMV–cerebellar signatures and further contextualizing the imaging-defined convergence node using AHBA-based transcriptomic mapping, this study aimed to clarify the systems-level involvement and normative molecular background of the DMV–cerebellar axis in body-first PD. These findings may help identify imaging markers associated with clinically defined PD subtypes and provide insights into subtype-related network organization.

Results

Clinical characteristics of the study cohort

84 participants were enrolled, including 54 patients with PD and 30 HCs. In the body-first group, probable RBD preceded motor symptom onset (n = 24); in the brain-first group, probable RBD emerged after motor onset (n = 30). MRI and clinical questionnaire data were obtained from all participants.

Demographic and clinical characteristics are summarized in Table 1. The three groups were comparable with respect to sex distribution, age, BMI, mean FD, and global cognitive performance assessed by the MMSE (all $P > 0.05$). Within the PD cohort, disease duration, LEDD, H-Y stage and PDQ-39 scores did not differ at the specified significance threshold. The body-first group had higher Unified Parkinson's Disease Rating Scale (UPDRS) total scores (56.58 ± 17.73 versus 44.63 ± 14.31; $P = 0.0083$) and UPDRS III scores (39.08 ± 11.04 versus 29.73 ± 9.94; $P = 0.0019$) than the brain-first group.

Body-first PD also showed greater non-motor burden, with higher Non-Motor Symptoms Questionnaire (NMSQ) scores ($P < 0.0001$), lower Parkinson's Disease Sleep Scale (PDSS) scores ($P = 0.0091$), and higher depression and anxiety scores than brain-first PD (Hamilton Depression Rating Scale, $P = 0.0466$; Hamilton Anxiety Rating Scale, $P = 0.0234$). Both PD groups had higher RBD Screening Questionnaire (RBDSQ) scores than controls, without a significant difference between the PD groups.

Table 1 near here

DMV connectivity differs between the clinical phenotypes

Relative to healthy controls, body-first PD showed increased DMV-seeded FC in bilateral cerebellar lobules VIII, IX and X and vermal lobules VIII and IX, together with decreased FC in the left middle occipital and superior parietal gyri (Fig. 1A). Brain-first PD showed decreased DMV-seeded FC in frontal motor-related regions; no cerebellar cluster survived the predefined corrected threshold in this comparison with controls (Fig. 1B)

Direct comparison between PD subtypes revealed that the body-first group showed significantly stronger DMV connectivity with bilateral cerebellar lobules VIIb, VIII, IX, and X, Crus II, and vermal lobules VIII and IX, as well as the right inferior temporal gyrus, relative to the brain-first group (Fig. 1C). Detailed whole-brain cluster information is provided in Supplementary Table 1. The preferential cerebellar

connectivity pattern remained evident in the PD-only sensitivity analysis that additionally adjusted for disease duration, LEDD and UPDRS III scores (Supplementary Fig. 2).

Fig. 1 near here

Cerebellar local functional measures show convergent alterations

Body-first PD showed higher ReHo than controls in bilateral cerebellar lobules IV–V, VI, VIII, IX and X and vermal lobules IV–V, VI, VII, VIII and IX. Lower ReHo was observed in bilateral frontal regions, including prefrontal cortex and the supplementary motor area (SMA; Fig. 2A). Brain-first PD showed more circumscribed increases in ReHo in the right cingulate gyrus, bilateral caudate nuclei and hippocampi, with decreased ReHo in the right inferior occipital gyrus (Fig. 2B).

Compared with brain-first PD, body-first PD showed higher ReHo in bilateral cerebellar lobules VI, VIII and IX, Crus II and left Crus I, as well as bilateral lingual gyri, left occipital cortex and right calcarine cortex. Lower ReHo was observed in bilateral superior and middle frontal gyri, the SMA, and right precentral and postcentral gyri (Fig. 2C). Thus, increased cerebellar synchrony coexisted with reduced synchrony in frontal motor-related regions.

A parallel pattern was observed in the ALFF analysis. Relative to HCs, body-first PD showed higher ALFF in bilateral lobule VIII and Crus II, bilateral superior frontal

gyri, paracentral lobules and postcentral gyri, and occipital and temporal cortices. Lower ALFF was observed in bilateral precuneus and posterior cingulate cortex, calcarine cortex, angular gyri and the right putamen (Fig. 2D). Brain-first PD showed predominantly frontal ALFF increases, with no cerebellar cluster surviving the corrected threshold relative to controls (Fig. 2E).

The direct PD-group comparison showed higher ALFF in body-first PD across cerebellar territories including bilateral lobules VII and VIII and Crus II, right lobules IV–V and VI and Crus I, and vermis VIII. Higher ALFF also involved bilateral precentral gyri, paracentral lobules and the SMA. Lower ALFF involved bilateral precuneus and calcarine cortex, the right lingual gyrus and left cuneus (Fig. 2F). All reported voxel-wise ReHo and ALFF findings met the same GRF thresholds as the FC analysis; cluster details are provided in Supplementary Table 2.

Fig. 2 near here

Lobule VIII combines functional alterations with lower gray matter volume

Given the convergent whole-brain findings implicating posterior cerebellar regions, we next examined cerebellar structural alterations and ROI-level convergence with a focus on bilateral lobule VIII (Fig. 3). Detailed comparisons across cerebellar subregions are shown in Supplementary Table 3. HC-referenced GMV overview showed that the body-first group exhibited more negative Z-scores across the majority

of cerebellar subregions than the brain-first group, indicating lower HC-referenced cerebellar GMV across multiple subregions, whereas the brain-first group remained relatively close to the HC reference level (Fig. 3A).

ROI-level characterization further identified bilateral lobule VIII as a common cerebellar node linking these structural and functional abnormalities. DMV–lobule VIII FC differed significantly across groups (Fig. 3B). Mean lobule VIII ALFF also showed a significant group effect, driven by higher values in body-first than brain-first PD (Fig. 3C). Similarly, mean lobule VIII ReHo differed across groups, with body-first PD showing higher values than both brain-first PD and HCs (Fig. 3D). After FDR correction across all three ROI outcomes, the omnibus effects remained significant for FC and ReHo. Detailed statistics are provided in Supplementary Tables 4 and 5.

Lobule VIII structure–function decoupling

We next quantified structure–function decoupling in bilateral lobule VIII using HC-referenced decoupling indices. The ALFF-based decoupling index differed significantly across groups. Post hoc analyses showed that body-first PD exhibited higher DI_ALFF than both brain-first PD ($P < 0.001$) and HCs ($P = 0.014$), whereas brain-first PD showed lower values than HCs (Fig. 3E). A similar pattern was observed for the ReHo-based decoupling index. Body-first PD showed significantly higher DI_ReHo than brain-first PD ($P < 0.001$) and HCs ($P < 0.001$), while the difference between brain-first PD and HCs did not reach significance (Fig. 3F). Both decoupling indices showed significant overall group effects after FDR correction. Detailed

statistics are provided in Supplementary Table 6.

Fig. 3 near here

DMV connectivity is associated with clinical burden after adjustment

In the combined PD cohort (n = 54), higher DMV–lobule VIII FC was associated with higher Freezing of Gait Questionnaire (FOG-Q) scores (standardized $\beta = 0.635$, $q < 0.001$), UPDRS III total scores ($\beta = 0.907$, $q < 0.001$) and NMSQ scores ($\beta = 0.657$, $q < 0.001$; Fig. 4A–C). Higher FC was associated with lower PDSS scores ($\beta = -0.795$, $q < 0.001$), indicating poorer sleep (Fig. 4D).

The regression models adjusted for age, sex, disease duration, LEDD, mean FD and clinical group. FDR correction covered the five tested clinical outcomes. The UPDRS III item 12 association and complete regression and partial correlation results are reported in Supplementary Table 7. These associations suggest that the connectivity measure contains information about clinical burden beyond the categorical grouping, while remaining observational associations within the discovery cohort.

Fig. 4 near here

Normative transcriptomic enrichment provides regional molecular context

To characterize the normative molecular context of the imaging-defined

convergence node, bilateral cerebellar lobule VIII was mapped to the Allen Human Brain Atlas (Fig. 5A). Using the top 300 lobule VIII-enriched genes as the primary threshold, GO biological process analysis identified significant enrichment of neural crest cell development and negative regulation of signal transduction (both FDR = 0.045; Fig. 5B). Sensitivity analyses across alternative gene-set thresholds showed additional developmental enrichment at the top 100 threshold, no FDR-significant terms at the top 200 threshold, and persistent enrichment of negative regulation of signal transduction at the top 500 threshold (FDR = 0.030; Fig. 5C). These findings provide exploratory normative transcriptomic context for lobule VIII as a multimodal imaging convergence node in body-first PD. Detailed enrichment results are provided in Supplementary Table 8.

Fig. 5 near here

Combined imaging measures improve exploratory within cohort discrimination

DMV–lobule VIII FC alone showed moderate discrimination between body-first and brain-first PD, with an AUC of 0.779 (95% CI, 0.641–0.903). Adding ALFF- and ReHo-based structure–function decoupling indices increased the AUC to 0.929 (95% CI, 0.849–0.988). The AUC increase was significant (ΔAUC = 0.150; paired-bootstrap 95% CI, 0.028–0.279; P = 0.014), with a consistent result obtained using the DeLong

test (P = 0.020; Fig. 6A). Model 2 also showed higher sensitivity, specificity, accuracy, and balanced accuracy than Model 1 (Fig. 6B). Standardized logistic regression coefficients were largest for DI_ALFF, followed by DMV–lobule VIII FC and DI_ReHo (Fig. 6C). Detailed classification metrics are provided in Supplementary Table 9.

Fig. 6 near here

Discussion

In this case-control study, we provide *in vivo* neuroimaging evidence for a subtype-specific brainstem–cerebellar signature in body-first PD. We found that body-first PD showed preferential enhancement of DMV–cerebellar functional connectivity, a pattern that was not observed in brain-first PD. Convergent multimodal analyses further identified bilateral cerebellar lobule VIII as a core cerebellar node, showing abnormal DMV coupling, increased regional synchronization and spontaneous activity, and more pronounced structural involvement in body-first PD. In addition, body-first PD exhibited marked lobule VIII structure–function decoupling, indicating a mismatch between reduced gray matter integrity and relatively preserved or increased functional measures. Importantly, DMV–lobule VIII connectivity was associated with gait, motor, non-motor, and sleep burden after covariate adjustment, and its combination with decoupling indices improved exploratory subtype discrimination. Together, these

findings support a DMV-centered cerebellar network abnormality associated with the clinically defined body-first phenotype and highlight bilateral lobule VIII as a convergence node linking subtype-related network alterations with clinically relevant disease burden.

The selective enhancement of DMV–cerebellar connectivity in clinically defined body-first PD suggests preferential involvement of brainstem-centered network organization in this phenotype. As an early site implicated in Lewy pathology and a key autonomic relay within the vagal system, the DMV represents a biologically plausible node for investigating brainstem-related network alterations in clinically defined body-first PD [7,28,32]. In this context, the present whole-brain connectivity findings suggest that abnormal DMV-related network involvement in body-first PD is not restricted to autonomic brainstem nuclei, but extends to cerebellar territories implicated in posture, gait, and sensorimotor integration. By contrast, brain-first PD showed a different pattern, characterized more by reduced DMV connectivity with frontal motor-related regions than by cerebellar involvement. This divergence supports the view that body-first and brain-first PD are not simply distinguished by symptom chronology, but may also differ at the level of large-scale network organization [33]. Rather than reflecting a nonspecific disease effect, the preferential DMV–cerebellar coupling observed here points to a subtype-related circuit signature that is more compatible with body-first pathophysiology.

A major strength of the present study is that the whole-brain findings were not left at the level of broad cerebellar involvement, but were further anchored to a specific

cerebellar node. Across functional connectivity, ReHo, ALFF, and structural analyses, bilateral lobule VIII emerged as the most consistent region of multimodal convergence. This is particularly meaningful because lobule VIII occupies a functionally relevant position within the posterior cerebellum and has been implicated in axial motor control, gait coordination, and sensorimotor processing [34-36]. In the current dataset, body-first PD showed stronger DMV–lobule VIII connectivity together with higher lobule VIII ALFF and ReHo, while the structural overview indicated more extensive cerebellar GMV reduction relative to the brain-first group. Thus, lobule VIII does not appear to be an incidental regional finding, but rather a core cerebellar node at which subtype-specific brainstem-related, functional, and structural abnormalities converge. This regional anchoring substantially strengthens the interpretability of the study by moving the findings beyond descriptive whole-brain contrasts toward a more mechanistically coherent network model.

The finding of elevated lobule VIII decoupling indices in body-first PD provides an additional level of biological interpretation. In the present study, body-first PD showed not only greater structural involvement within lobule VIII, but also relatively increased functional activity and local synchrony, resulting in a pronounced structure–function mismatch. This pattern suggests that cerebellar dysfunction in body-first PD cannot be understood as simple atrophy alone, nor as straightforward functional compensation [37-39]. Instead, it may reflect an abnormal network state in which structurally vulnerable tissue remains functionally overengaged or dysregulated. This pattern may reflect disproportionate functional engagement relative to regional

structural integrity. However, the cross-sectional data cannot determine whether the functional abnormality is compensatory, maladaptive, or secondary to upstream network perturbation [37,40]. Importantly, this decoupling pattern was much more evident in body-first than in brain-first PD, supporting the notion that cerebellar vulnerability differs across subtypes. Although the present study is imaging-based and cannot establish mechanism directly, the decoupling results suggest that body-first PD involves not only stronger cerebellar participation, but also a qualitatively different relationship between cerebellar structure and function.

Another important implication of the present findings is their multidomain clinical relevance. After adjustment for age, sex, disease duration, LEDD, mean FD, and group, stronger DMV–lobule VIII connectivity remained associated with greater gait impairment, worse motor severity, higher non-motor burden, and poorer sleep quality. This pattern is notable because it suggests that the DMV–lobule VIII circuit is not linked to a single isolated symptom, but may instead represent a shared network substrate spanning multiple clinically relevant domains. In body-first PD, where autonomic and sleep-related disturbances often emerge early and axial motor symptoms become increasingly prominent, such a circuit may help bridge the gap between brainstem-centered pathology and broader symptom expression [19,41-43]. The association with FOG-Q and UPDRS III is particularly consistent with a role for cerebellar dysfunction in gait and axial motor control [44], whereas the associations with NMSQ and PDSS extend the significance of this circuit beyond motor function alone. Taken together, these results support the view that DMV–lobule VIII abnormalities are

clinically meaningful rather than merely imaging-defined subgroup markers, and may capture an integrated burden of motor and non-motor dysfunction in PD.

The AHBA-based analysis provided a normative molecular annotation layer for the imaging-defined lobule VIII convergence node [45]. Genes relatively enriched in lobule VIII were overrepresented in neural crest cell development and negative regulation of signal transduction, with the latter remaining evident in the top 500-gene sensitivity analysis. Although AHBA does not provide patient-specific transcriptomic evidence, these findings suggest that lobule VIII is embedded within a distinct molecular architecture involving developmental patterning and signal-regulatory programs. The developmental enrichment may reflect region-specific molecular identity [45,46], whereas the signal-transduction-related enrichment is mechanistically relevant because neuronal signaling cascades regulate neuronal responsiveness, synaptic modulation, intracellular feedback, and activity-dependent plasticity [47-49]. In the context of body-first PD, this normative molecular background supports the biological plausibility of lobule VIII as a cerebellar node susceptible to DMV-related network perturbation. Together with the multimodal convergence of enhanced DMV-seeded connectivity, increased ALFF and ReHo, gray matter involvement, and structure–function decoupling, these findings provide normative molecular context for lobule VIII and suggest that its regional expression profile includes developmental and signal-regulatory programs potentially relevant to its functional organization [40,50]. Because AHBA is derived from neurotypical postmortem donors, these findings should be interpreted as normative molecular context rather than patient-specific evidence of

altered gene expression.

The exploratory classification analysis further suggests that DMV–lobule VIII imaging markers may have potential stratification value. DMV–lobule VIII connectivity alone showed moderate cross-validated discrimination between body-first and brain-first PD, whereas adding lobule VIII decoupling indices significantly increased the AUC from 0.779 to 0.929. The AUC increase was supported by both paired bootstrap analysis and the DeLong test, although the classification findings remain exploratory in the absence of external validation. Although these results should be interpreted cautiously, they indicate that multimodal cerebellar markers may provide more informative subtype-related signatures than a single connectivity measure alone. This is conceptually important because biological stratification in PD is unlikely to be captured by one isolated feature; rather, it may require combined markers that reflect both network coupling and downstream regional consequences [51,52]. In this regard, the improved performance observed when decoupling measures were incorporated is consistent with the broader interpretation of body-first PD as a disorder involving coordinated abnormalities in DMV-centered connectivity, cerebellar activity, and structural vulnerability. These findings therefore support the potential translational relevance of the DMV–lobule VIII circuit, while remaining appropriately exploratory at the current stage.

This study has several limitations. First, the single-center, cross-sectional design and modest sample size limit generalizability and preclude inference regarding disease progression. Second, subtype assignment was based on the temporal relationship

between probable RBD and motor onset without polysomnographic confirmation in all participants, which may introduce misclassification. Third, the small size of the DMV makes functional connectivity estimates susceptible to partial-volume and physiological noise effects. Fourth, the exploratory classification analysis was derived from the same cohort and lacked external validation. Finally, AHBA analyses were based on normative postmortem expression data and should not be interpreted as patient-specific transcriptional alterations. Larger multicenter longitudinal studies with independent validation are warranted.

In conclusion, clinically defined body-first PD was associated with a distinct DMV-centered cerebellar network pattern characterized by enhanced DMV–cerebellar coupling, altered lobule VIII functional activity, lower regional GMV, and greater structure–function mismatch. The association of DMV–lobule VIII connectivity with motor and non-motor burden further supports the clinical relevance of this network. These findings identify the DMV–cerebellar axis as a candidate systems-level network signature associated with the body-first phenotype and warrant validation in longitudinal and independent cohorts.

Methods

Study participants

This observational case-control study included 54 patients with PD and 30 healthy controls recruited at the Affiliated Brain Hospital of Nanjing Medical University. Patients fulfilled the Movement Disorder Society Clinical Diagnostic Criteria for PD

and had Mini-Mental State Examination scores > 17. Exclusion criteria were other major neurological or psychiatric disorders, MRI contraindications, severe ocular disease, inability to walk independently, and an uncertain temporal relationship between RBD and motor symptom onset. All patients were clinically assessed and scanned after overnight withdrawal of antiparkinsonian medication (OFF-medication state, ≥12 h).

Patients were assigned to the body-first group when probable RBD preceded motor symptom onset and to the brain-first group when probable RBD emerged after motor onset, based on the temporal relationship between probable RBD and motor symptom onset. Probable RBD was defined according to the International Classification of Sleep Disorders, Third Edition (ICSD-3) criteria using the REM Sleep Behavior Disorder Screening Questionnaire (RBDSQ) [8,10,13,14], with a cutoff score of ≥6 [53]. Because polysomnography was not available for all participants, RBD was designated probable rather than polysomnography-confirmed. These labels describe clinically defined phenotypes. The final groups comprised 24 body-first and 30 brain-first patients.

The protocol was approved by the hospital ethics committee (approval no. 2022-KY054-01) and conducted in accordance with the 2013 Declaration of Helsinki. All participants provided written informed consent. Data were anonymized before analysis, and participant privacy was protected.

Clinical assessments

Two experienced neurologists independently performed clinical assessments, resolving discrepancies by consensus. Measures included UPDRS parts I–IV, RBDSQ, FOG-Q, Hamilton Depression Rating Scale, Hamilton Anxiety Rating Scale, NMSQ, PDSS, Mini-Mental State Examination and Parkinson's Disease Questionnaire-39. The clinical association analyses used FOG-Q, UPDRS III total, UPDRS III item 12, NMSQ and PDSS. Higher PDSS scores indicate better sleep.

MRI acquisition and preprocessing

MRI was acquired on a 3.0-T Siemens Verio scanner with an eight-channel radiofrequency coil at the Affiliated Brain Hospital of Nanjing Medical University. T1-weighted images were obtained with a three-dimensional magnetization-prepared rapid gradient-echo sequence: repetition time (TR), 2,000 ms; echo time (TE), 3.34 ms; flip angle, 7°; 128 sagittal slices; slice thickness, 1.33 mm; and matrix, 256 × 256.

Resting-state functional images were acquired with a T2*-weighted single-shot gradient-echo echo-planar imaging sequence: 240 volumes; TR, 2000 ms; TE, 30 ms; field of view, 240 × 240 mm; matrix, 64 × 64; flip angle, 90°; 30 axial slices; slice thickness, 3.0 mm; and no interslice gap.33 These field-of-view and matrix settings correspond to native in-plane sampling of 3.75 × 3.75 mm. Participants lay supine with their eyes closed and were instructed to remain awake, minimize head movement and avoid deliberate cognitive activity.

DICOM images were converted to NIfTI format with dcm2niix and visually inspected in MRIcroGL. Preprocessing used SPM12 and DPABI v6.0 in MATLAB

R2021a. The first 20 volumes were discarded, leaving 220 volumes for analysis. Images underwent slice-timing correction and realignment. Participants with translation > 2.0 mm or rotation > 2° in any direction were excluded. Functional images were coregistered to each participant's T1-weighted image, normalized to Montreal Neurological Institute (MNI) space and resampled to 3 × 3 × 3 mm voxels.

Linear trends and nuisance signals were removed before analysis-specific temporal processing. Nuisance regressors comprised the Friston 24 motion parameters, mean white matter and cerebrospinal fluid signals, global signal, and censored volumes identified by framewise displacement (FD) >0.5 mm. ALFF was calculated from the detrended, nuisance-regressed time series before temporal band-pass filtering, by applying a fast Fourier transform and averaging the square root of the power spectrum within 0.01–0.08 Hz. For FC and ReHo analyses, the nuisance-regressed time series were band-pass filtered at 0.01–0.08 Hz. Spatial smoothing with a 6-mm full-width at half-maximum Gaussian kernel was applied. ReHo was calculated from spatially unsmoothed data, and the resulting standardized ReHo maps were subsequently smoothed. Mean FD was included as a covariate in group-level functional analyses.

DMV seed definition and functional connectivity

Whole-brain voxel-wise analyses were performed using SPM12 and DPABI V6.0 implemented in MATLAB R2021a, and statistical maps were visualized using BrainNet Viewer (version 1.7) [54].

For seed-based functional connectivity (FC) analysis, the bilateral DMV was

manually delineated in MNI space with reference to the Allen Human Brain Atlas and an established brainstem atlas [45,55], centered approximately at MNI coordinates (±4, −37, −54). ROI delineation was jointly performed by two experienced neurologists and one anatomy expert, and the final seed mask was established by consensus. To minimize contamination from adjacent cerebrospinal fluid spaces and vascular or non-neuronal structures, the ROI was restricted to the medullary parenchyma. The bilateral DMV mask was delineated on a 1 × 1 × 1 mm isotropic grid in MNI space and resampled to the 3 × 3 × 3 mm functional grid using nearest-neighbor interpolation. After resampling, the bilateral mask contained 12 voxels in total, corresponding to a volume of 324 mm^3. The anatomical location of the DMV seed is shown in Supplementary Fig. 1. Potential CSF overlap was quantified using participant-specific CSF probability maps in the same MNI space as the DMV seed. Probabilities were sampled at seed voxel centers using trilinear interpolation. For each participant, we calculated the percentage of seed voxels with a CSF probability ≥0.5 and the mean CSF probability across the seed (Supplementary Fig. 3). For each participant, the mean time series of the bilateral DMV seed was extracted, and voxel-wise Pearson correlation coefficients were calculated between the seed time series and all other brain voxels. Correlation coefficients were then transformed into Fisher's z values to generate individual zFC maps.

ALFF and ReHo estimation

ALFF was calculated by transforming each voxel's preprocessed time series into the frequency domain with a fast Fourier transform and averaging the square root of the

power spectrum within 0.01–0.08 Hz. Individual ALFF maps were standardized to zALFF maps. ReHo was calculated using Kendall's coefficient of concordance among 27 voxels (the center voxel and its 26 nearest neighbors), then standardized to zReHo maps and spatially smoothed as described above.

Whole brain group comparisons

Voxel-wise analysis of covariance (ANCOVA) assessed group differences in zFC, zALFF and zReHo across body-first PD, brain-first PD and controls. Age, sex and mean FD were covariates. Tukey–Kramer post hoc comparisons were applied where appropriate. GRF correction used a voxel-level threshold of $P < 0.001$ and a cluster-level threshold of $P < 0.05$. Maps were generated in SPM12 and DPABI and visualized with BrainNet Viewer v1.7.35

A sensitivity analysis restricted to patients with PD compared body-first and brain-first FC maps after adjustment for age, sex, mean FD, disease duration, LEDD and UPDRS III scores. The same GRF thresholds were used.

Cerebellar structure and regional measures

Cerebellar GMV was analyzed with the SUIT toolbox in SPM12.36–37 The cerebellum was isolated from supratentorial structures and segmented into gray matter, white matter and cerebrospinal fluid. Gray matter maps were normalized to the SUIT template using diffeomorphic anatomical registration through exponentiated Lie algebra, modulated to preserve tissue amount, and smoothed with a 4-mm FWHM

Gaussian kernel. Mean regional GMV and total cerebellar GMV were extracted using the SUIT atlas.

Regional GMV comparisons used ANCOVA in SPSS v27.0 with age, sex and total intracranial volume (TIV) as covariates. Pairwise comparisons of estimated marginal means used Bonferroni correction, with a significance threshold of $P < 0.001$ for regional comparisons. For descriptive characterization, regional GMV was also standardized relative to controls [56-58]:

$$Z_{i,j} = \frac{V_{i,j} - \mu_{HC,j}}{\sigma_{HC,j}}$$

Here, $V_{I,j}$ represents the raw gray matter volume of subject i in subregion j, while $\mu_{HC,j}$ and $\sigma_{HC,j}$ denote the mean and standard deviation of the HC group in that subregion, respectively. Lower Z-scores indicate more severe atrophy relative to the normal baseline. Based on convergent whole-brain findings, bilateral cerebellar lobule VIII was selected as the primary ROI for subsequent region-based analyses.

Bilateral lobule VIII was selected for subsequent ROI analyses after inspection of convergent whole-brain findings. DMV – lobule VIII FC and mean lobule VIII ALFF and ReHo were extracted for each participant. Group comparisons used ANCOVA with age, sex and mean FD, followed by Tukey-adjusted comparisons of estimated marginal means. FDR correction covered the three ROI outcomes. These analyses characterize a discovery-defined region and were treated as follow-up analyses rather than independent confirmatory tests.

Structure–function decoupling analysis

To quantify cerebellar structure–function decoupling, a bilateral cerebellar lobule VIII GMV measure was first adjusted for total intracranial volume (TIV) using a linear regression model derived from the healthy control group. The adjusted GMV values were then standardized relative to the HC to generate HC-referenced z-scores:

$$zGMV_{HC} = \frac{GMV_{adj} - \mu_{GMV,\,HC}}{\sigma_{GMV,HC}}$$

$$zALFF_{HC} = \frac{ALFF - \mu_{ALFF,\,HC}}{\sigma_{ALFF,\,HC}}$$

$$zReHo_{HC} = \frac{ReHo - \mu_{ReHo,\,HC}}{\sigma_{ReHo,\,HC}}$$

Where $zGMV_{\mathrm{adj}}$ denotes the TIV-adjusted gray matter volume of bilateral cerebellar lobule VIII for an individual participant; $ALFF$ and $ReHo$ denote the individual mean ALFF and mean ReHo values extracted from bilateral cerebellar lobule VIII; $\mu_{GMV,HC}$, $\mu_{ALFF,HC}$ and $\mu_{ReHo,HC}$ represent the corresponding mean values in the HC group; and $\sigma_{GMV,HC}$, $\sigma_{ALFF,HC}$ and $\sigma_{ReHo,HC}$ denote the corresponding standard deviations in the HC group.

Two decoupling indices were defined as [59-61]:

$$DI_{ALFF} = zALFF_{HC} - zGMV_{HC}$$

$$DI_{ReHo} = zReHo_{HC} - zGMV_{HC}$$

Where DI_{ALFF} and DI_{ReHo} respectively indicate the ALFF-based and ReHo-based structure–function decoupling indices. A higher decoupling index indicated a greater mismatch between functional abnormality and structural alteration, that is, relatively increased functional activity or synchronization in the context of reduced gray matter volume. Group differences in DI_{ALFF} and DI_{ReHo} were assessed using ANCOVA with

age, sex, and mean FD as covariates, followed by Tukey-adjusted pairwise comparisons. FDR correction was applied across the two decoupling outcomes. Here, structure–function decoupling was operationalized as an HC-referenced regional mismatch between lobule VIII gray matter volume and local ALFF/ReHo measures, rather than connectome-level coupling between structural and functional connectivity.

Clinical association analyses

Clinical associations were tested in the combined PD cohort (n = 54). Separate multivariable linear regression models assessed DMV – lobule VIII FC in relation to FOG-Q, UPDRS III total, UPDRS III item 12, NMSQ and PDSS. Covariates were age, sex, disease duration, LEDD, mean FD and clinical group. Standardized coefficients were obtained from z-scored variables. Partial correlations were calculated as a sensitivity analysis using residuals after adjustment for the same covariates. FDR correction was applied across the five clinical outcomes separately within each analytic approach. The scatter plots display residualized variables after covariate adjustment.

AHBA-based transcriptomic contextualization

An exploratory AHBA analysis compared expression in bilateral lobule VIII with the remaining cerebellum [45,62]. A two-label atlas was generated in MNI space, with lobule VIII assigned label 1 and the remaining cerebellum label 2. This anatomical comparison provided normative regional context for the imaging finding; it did not use

patient transcriptomic measurements or estimate imaging–gene associations across participants.

AHBA microarray data were processed with abagen using a standardized imaging-transcriptomic workflow [63,64]. Steps included probe reannotation, intensity-based filtering, differential-stability-based probe selection, sample-wise and gene-wise normalization, and donor-wise regional aggregation. The intensity filtering threshold was 0.5. Scaled robust sigmoid normalization was applied at the sample and gene levels, and regional expression was averaged across donors. Missing-region interpolation was not used; only directly assigned tissue samples were included. The final assignment contained 52 tissue samples in bilateral lobule VIII and 224 in the remaining cerebellum. These counts refer to postmortem AHBA sampling sites, not participants in the clinical cohort.

The resulting region-by-gene expression matrix was used to rank genes according to their relative enrichment in lobule VIII compared with the remaining cerebellum. The primary enrichment analysis was performed using the top 300 lobule VIII-enriched genes, while the top 100, 200, and 500 genes were examined as sensitivity thresholds. Functional enrichment analyses were performed using Enrichr through the gseapy package, including Gene Ontology biological process, KEGG, Reactome, and disease-related gene-set libraries. Enrichment results were evaluated using FDR-corrected P values [65,66].

Exploratory subtype-classification analysis

An exploratory logistic regression framework was used to distinguish body-first from brain-first PD. Model 1 included DMV–cerebellar lobule VIII functional connectivity alone. Model 2 included DMV–cerebellar lobule VIII functional connectivity together with ALFF-based and ReHo-based cerebellar lobule VIII decoupling indices. Model performance was evaluated using repeated stratified 5-fold cross-validation, repeated 50 times. Feature normalization was performed within each training fold and subsequently applied to the corresponding test fold to avoid information leakage. Out-of-fold predicted probabilities were averaged across repetitions to obtain subject-level prediction scores. Receiver operating characteristic (ROC) curves and area under the curve (AUC) values were calculated, and 95% confidence intervals were estimated by bootstrap resampling. Sensitivity, specificity, accuracy, and balanced accuracy were computed using the optimal threshold determined by the Youden index. The difference in AUC between Models 1 and 2 was evaluated using stratified paired bootstrap resampling at the participant level (10,000 iterations), with paired predictions preserved within each participant. The DeLong test for correlated ROC curves was additionally performed as a sensitivity analysis. These analyses were performed in Python (version 3.10) using custom scripts.

Statistical analysis

Demographic and baseline clinical variables were analyzed using SPSS (version 27.0) and GraphPad Prism (version 9). Data normality was assessed using Q-Q plots and histograms. Normally distributed continuous variables are presented as mean ±

standard deviation (SD), whereas non-normally distributed variables are presented as median (interquartile range). Categorical variables were compared using the chi-square test, and continuous variables were compared using one-way ANOVA or nonparametric tests, as appropriate, followed by Tukey-adjusted post hoc comparisons when applicable. Whole-brain voxel-wise analyses were performed in SPM12 and DPABI V6.0 implemented in MATLAB R2021a, cerebellar GMV preprocessing was performed using the SUIT toolbox in SPM12, and ROI-level characterization, structure–function decoupling, multivariable regression, partial correlation, and exploratory classification analyses were implemented in Python using custom scripts. Unless otherwise specified, all tests were two-sided, and $P < 0.05$ was considered statistically significant.

Data availability

The datasets generated during and analysed during the current study are available from the corresponding author on reasonable request.

Code availability

The custom analysis scripts used in this study are available from the corresponding author on reasonable request.

References

1 Morris, H. R., Spillantini, M. G., Sue, C. M. & Williams-Gray, C. H. The pathogenesis of Parkinson's disease. *Lancet* **403**, 293-304 (2024).

2 Taimur, M. *et al.* Frequency of Cognitive Impairment in Patients with Parkinson's Disease. *Cureus* **11**, e4733 (2019).

3 Huang, B. *et al.* Gut microbiome dysbiosis across early Parkinson's disease, REM sleep behavior disorder and their first-degree relatives. *Nat Commun* **14**, 2501 (2023).

4 Bloem, B. R., Okun, M. S. & Klein, C. Parkinson's disease. *Lancet* **397**, 2284-2303 (2021).

5 Dorsey, E. R., De Miranda, B. R., Horsager, J. & Borghammer, P. The Body, the Brain, the Environment, and Parkinson's Disease. *J Parkinsons Dis* **14**, 363-381 (2024).

6 Kim, M. S., Park, D. G., Shin, I. J., An, Y. S. & Yoon, J. H. Gastric emptying time and its correlation with cardiac MIBG in body-first and brain-first subtype Parkinson's disease. *J Neurol* **272**, 28 (2024).

7 Horsager, J. *et al.* Brain-first versus body-first Parkinson's disease: a multimodal imaging case-control study. *Brain* **143**, 3077-3088 (2020).

8 Schröter, N. *et al.* Amygdala neurodegeneration differentiates brain-first and body-first Parkinson's disease: An MRI study. *Parkinsonism Relat Disord* **135**, 107827 (2025).

9 Nagaraj, T. *et al.* Temporal onset of non-motor symptoms and the body-first/brain-first dichotomy in Parkinson's disease: a cross-sectional single center experience. *J Neural Transm (Vienna)* (2025).

10 Borghammer, P. & Van Den Berge, N. Brain-First versus Gut-First Parkinson's Disease: A Hypothesis. *J Parkinsons Dis* **9**, S281-s295 (2019).

11 Sola, P. *et al.* Neuroprotective approaches to halt Parkinson's disease progression. *Neurochem Int* **158**, 105380 (2022).

12 Tysnes, O. B., Müller, B. & Larsen, J. P. Are dysautonomic and sensory symptoms present in early Parkinson's disease? *Acta Neurol Scand Suppl*, 72-77 (2010).

13 Pavelka, L. *et al.* Body-First Subtype of Parkinson's Disease with Probable REM-Sleep Behavior Disorder Is Associated with Non-Motor Dominant Phenotype. *J Parkinsons Dis* **12** (2022).

14 Borghammer, P. *et al.* Neuropathological evidence of body-first vs. brain-first Lewy body disease. *Neurobiol Dis* **161**, 105557 (2021).

15 Dauvilliers, Y. *et al.* REM sleep behaviour disorder. *Nat Rev Dis Primers* **4**, 19 (2018).

16 Muntean, M. L., Sixel-Döring, F. & Trenkwalder, C. REM sleep behavior disorder in Parkinson's disease. *J Neural Transm (Vienna)* (2014).

17 Ma, L. *et al.* Detection of Motor Dysfunction With Wearable Sensors in Patients With Idiopathic Rapid Eye Movement Disorder. *Front Bioeng Biotechnol* **9**, 627481 (2021).

18 Dong, S. *et al.* Comparison of vagus nerve cross-sectional area between brain-first and body-first Parkinson's disease. *NPJ Parkinsons Dis* **10**, 231 (2024).

19 Horsager, J. & Borghammer, P. Brain-first vs. body-first Parkinson's disease: An update on recent evidence. *Parkinsonism Relat Disord* **122**, 106101 (2024).

20 Travagli, R. A. & Anselmi, L. Vagal neurocircuitry and its influence on gastric motility. *Nat Rev Gastroenterol Hepatol* **13**, 389-401 (2016).

21 Braak, H., Rüb, U., Gai, W. P. & Del Tredici, K. Idiopathic Parkinson's disease: possible routes by which vulnerable neuronal types may be subject to neuroinvasion by an unknown pathogen. *J Neural Transm (Vienna)* **110**, 517-536 (2003).

22 Wang, Y. *et al.* Role of Corticotropin-Releasing Factor in Cerebellar Motor Control and Ataxia. *Curr Biol* **27**, 2661-2669 e2665 (2017).

23 Young, J. I. *et al.* Genome-wide brain DNA methylation analysis suggests epigenetic reprogramming in Parkinson disease. *Neurol Genet* **5**, e342 (2019).

24 Miwa, H., Kubo, T., Suzuki, A. & Kondo, T. Intragastric proteasome inhibition induces alpha-synuclein-immunopositive aggregations in neurons in the dorsal motor nucleus of the vagus in rats. *Neurosci Lett* **401**, 146-149 (2006).

25 Pan-Montojo, F. *et al.* Progression of Parkinson's disease pathology is reproduced by intragastric administration of rotenone in mice. *PLoS One* **5**, e8762 (2010).

26 Bove, C., Coleman, F. H. & Travagli, R. A. Characterization of the Basic Membrane Properties of Neurons of the Rat Dorsal Motor Nucleus of the Vagus in Paraquat-Induced Models of Parkinsonism. *Neuroscience* **418**, 122-132 (2019).

27 Zhang, X. Y. *et al.* A role for the cerebellum in motor-triggered alleviation of anxiety. *Neuron* **112**, 1165-1181 e1168 (2024).

28 Wang, R., Ren, H., Kaznacheyeva, E., Lu, X. & Wang, G. Association of Glial Activation and α-Synuclein Pathology in Parkinson's Disease. *Neurosci Bull* **39**, 479-490 (2023).

29 Goldberg, J. A. *et al.* Calcium entry induces mitochondrial oxidant stress in vagal neurons at risk in Parkinson's disease. *Nat Neurosci* **15**, 1414-1421 (2012).

30 Miyazaki, I. *et al.* Chronic Systemic Exposure to Low-Dose Rotenone Induced Central and Peripheral Neuropathology and Motor Deficits in Mice: Reproducible Animal Model of Parkinson's Disease. *Int J Mol Sci* **21** (2020).

31 Cheng, W. *et al.* Hindbrain circuits in the control of eating behaviour and energy balance. *Nat Metab* **4**, 826-835 (2022).

32 Kim, S. *et al.* Transneuronal Propagation of Pathologic α-Synuclein from the Gut to the Brain Models Parkinson's Disease. *Neuron* **103**, 627-641.e627 (2019).

33 Conti, M. *et al.* Cortical Functional Connectivity Changes in the Body-First and Brain-First Subtypes of Parkinson's Disease. *Mov Disord* **40**, 254-265 (2025).

34 Stoodley, C. J. & Schmahmann, J. D. Functional topography in the human cerebellum: a meta-analysis of neuroimaging studies. *Neuroimage* **44**, 489-501 (2009).

35 Stoodley, C. J., Valera, E. M. & Schmahmann, J. D. Functional topography of the cerebellum for motor and cognitive tasks: an fMRI study. *Neuroimage* **59**, 1560-1570 (2012).

36 Pijpers, A., Winkelman, B. H., Bronsing, R. & Ruigrok, T. J. Selective impairment of the cerebellar C1 module involved in rat hind limb control reduces step-dependent modulation of cutaneous reflexes. *J Neurosci* **28**, 2179-2189 (2008).

37 Zarkali, A. *et al.* Organisational and neuromodulatory underpinnings of structural-functional connectivity decoupling in patients with Parkinson's disease. *Communications Biology* **4**, 86 (2021).

38 Shang, S. *et al.* Optimization of structural connectomes and scaled patterns of structural-functional decoupling in Parkinson's disease. *Neuroimage* **284**, 120450 (2023).

39 Canu, E. *et al.* Brain structural and functional connectivity in Parkinson's disease with freezing of gait. *Hum Brain Mapp* **36**, 5064-5078 (2015).

40 Wu, T. & Hallett, M. The cerebellum in Parkinson's disease. *Brain* **136**, 696-709 (2013).

41 Raccagni, C. *et al.* Gait and postural disorders in parkinsonism: a clinical approach. *J Neurol* **267**, 3169-3176 (2020).

42 Xu, H. T. *et al.* Histaminergic Innervation of the Ventral Anterior Thalamic Nucleus Alleviates Motor Deficits in a 6-OHDA-Induced Rat Model of Parkinson's Disease. *Neurosci Bull* **41**, 551-568 (2025).

43 Huang, Y. *et al.* Glutamatergic Circuits in the Pedunculopontine Nucleus Modulate Multiple Motor Functions. *Neurosci Bull* **40**, 1713-1731 (2024).

44 Takakusaki, K. Functional Neuroanatomy for Posture and Gait Control. *J Mov Disord* **10**, 1-17 (2017).

45 Hawrylycz, M. J. *et al.* An anatomically comprehensive atlas of the adult human brain transcriptome. *Nature* **489**, 391-399 (2012).

46 Citri, A. & Malenka, R. C. Synaptic Plasticity: Multiple Forms, Functions, and Mechanisms. *Neuropsychopharmacology* **33**, 18-41 (2008).

47 Flavell, S. W. & Greenberg, M. E. Signaling mechanisms linking neuronal activity to gene expression and plasticity of the nervous system. *Annu Rev Neurosci* **31**, 563-590 (2008).

48 Laranjeira, C. & Pachnis, V. Enteric nervous system development: Recent progress and future challenges. *Autonomic Neuroscience* **151**, 61-69 (2009).

49 Nagy, N. & Goldstein, A. M. Enteric nervous system development: A crest cell's journey from neural tube to colon. *Semin Cell Dev Biol* **66**, 94-106 (2017).

50 Horsager, J. & Borghammer, P. Brain-first vs. body-first Parkinson's disease: An update on recent evidence. *Parkinsonism & Related Disorders* **122**, 106101 (2024).

51 Fereshtehnejad, S. M., Zeighami, Y., Dagher, A. & Postuma, R. B. Clinical criteria for subtyping Parkinson's disease: biomarkers and longitudinal progression. *Brain* **140**, 1959-1976 (2017).

52 Albrecht, F. *et al.* Unraveling Parkinson's disease heterogeneity using subtypes based on multimodal data. *Parkinsonism Relat Disord* **102**, 19-29 (2022).

53 Sun, J. *et al.* Disruption of locus coeruleus-related functional networks in Parkinson's disease. *NPJ Parkinsons Dis* **9**, 81 (2023).

54 Xia, M., Wang, J. & He, Y. BrainNet Viewer: a network visualization tool for human brain connectomics. *PLoS One* **8**, e68910 (2013).

55 *Duvernoy's Atlas of the Human Brain Stem and Cerebellum*. (AJNR Am J Neuroradiol. 2009 May;30(5):e75.).

56 Diedrichsen, J. A spatially unbiased atlas template of the human cerebellum. *Neuroimage* **33**, 127-138 (2006).

57 Diedrichsen, J., Balsters, J. H., Flavell, J., Cussans, E. & Ramnani, N. A probabilistic MR atlas of the human cerebellum. *Neuroimage* **46**, 39-46 (2009).

58 Tremblay, C. *et al.* Brain atrophy progression in Parkinson’s disease is shaped by connectivity and local vulnerability. *Brain Communications* **3** (2021).

59 Preti, M. G. & Van De Ville, D. Decoupling of brain function from structure reveals regional behavioral specialization in humans. *Nat Commun* **10**, 4747 (2019).

60 Krohn, S. *et al.* A spatiotemporal complexity architecture of human brain activity. *Sci Adv* **9**, eabq3851 (2023).

61 Baum, G. L. *et al.* Development of structure-function coupling in human brain networks during youth. *Proc Natl Acad Sci U S A* **117**, 771-778 (2020).

62 Sunkin, S. M. *et al.* Allen Brain Atlas: an integrated spatio-temporal portal for exploring the central nervous system. *Nucleic Acids Res* **41**, D996-d1008 (2013).

63 Markello, R. D. *et al.* Standardizing workflows in imaging transcriptomics with the abagen toolbox. *eLife* **10**, e72129 (2021).
64 Arnatkeviciute, A., Fulcher, B. D. & Fornito, A. A practical guide to linking brain-wide gene expression and neuroimaging data. *Neuroimage* **189**, 353-367 (2019).
65 Chen, E. Y. *et al.* Enrichr: interactive and collaborative HTML5 gene list enrichment analysis tool. *BMC Bioinformatics* **14**, 128 (2013).
66 Kuleshov, M. V. *et al.* Enrichr: a comprehensive gene set enrichment analysis web server 2016 update. *Nucleic Acids Res* **44**, W90-97 (2016).

Acknowledgements

This work was supported by grants 32030044, 82522033, and 82101332 from the National Natural Science Foundation of China; grant BK20240168 and BK20240307 from the Natural Science Foundation of Jiangsu Province, China; grant LNSN-202402 from the State Key Laboratory of Pharmaceutical Biotechnology; grants 020814380197 and 020814380208 from the Fundamental Research Funds for the Central Universities; grant 2024300475 from the Top Talents Program of Nanjing University Integrated Research Platform of the Ministry of Education; grant ZKX24054 from the Key Project of Nanjing Municipal Health Commission, China; grant 2024KF0242 from the Qilu Clinical Research Fund, Nanjing Medical University, China; and grant ZNJC202511 from the Translational Medicine and Interdisciplinary Research Joint Fund of Zhongnan Hospital of Wuhan University, China.

Author contributions

L.S. and Q.L. performed the data collection, imaging preprocessing, statistical analysis, and interpretation of results. **L.S.** drafted the manuscript. **Q.L.** contributed to methodological refinement and critical revision of the manuscript. **Y.X., S.L., G.H.,**

L.Z., H.W., and W.Y. contributed to data analysis, technical support, and manuscript revision. **L.W.** provided methodological guidance and assisted with study design. **S.F., J.Z., X.Z., and Y.P.** conceived and supervised the study. **J.Z., X.Z., and Y.P.** reviewed and revised the manuscript. All authors approved the final version of the manuscript.

Competing interests

The authors declare no competing financial interests and no conflicts of interest in the writing of this article.

Figure Legends

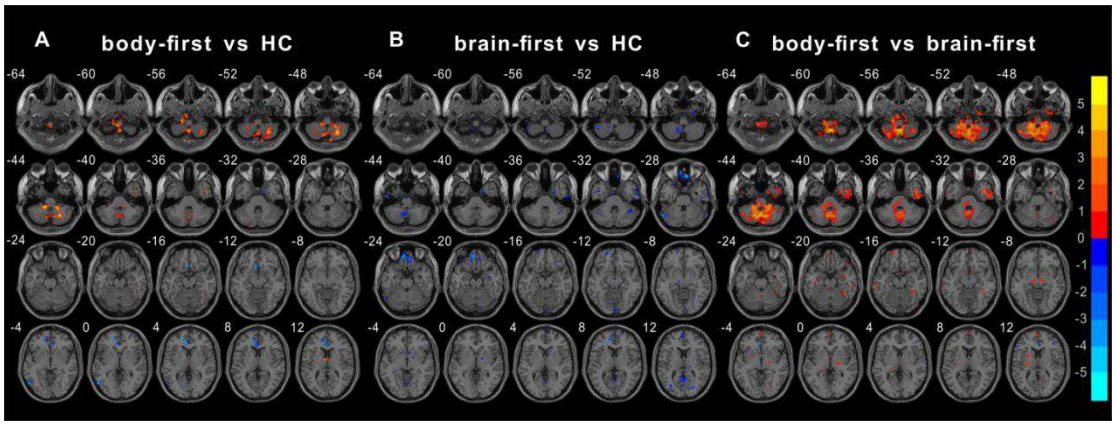


Fig. 1. Whole-brain DMV-seeded functional connectivity differences among body-first PD, brain-first PD, and healthy controls. (A) Body-first PD versus healthy controls. (B) Brain-first PD versus healthy controls. (C) Body-first PD versus brain-first PD. Warm colors indicate increased connectivity in the former group, and cool colors indicate decreased connectivity. Results were corrected using Gaussian random field theory (cluster-level $p < 0.05$, voxel-level $p < 0.001$). DMV, dorsal motor nucleus of the vagus; PD, Parkinson's disease; HC, healthy control.

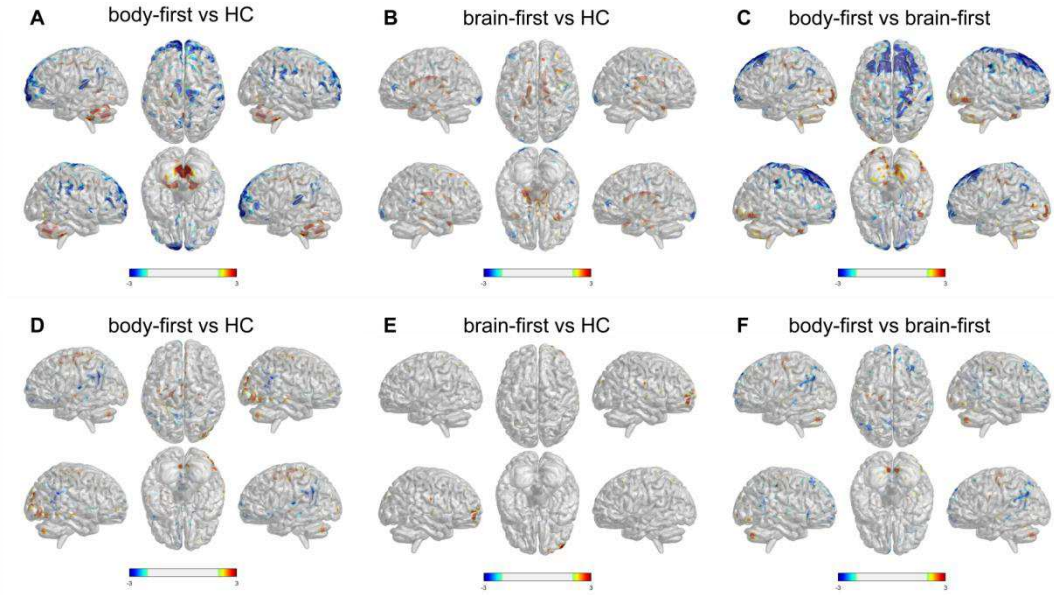


Fig. 2. Group differences in ReHo and ALFF among the body-first PD, brain-first PD, and HCs. (A) ReHo map for body-first PD versus HCs. (B) ReHo map for brain-first PD versus HCs. (C) ReHo map for body-first PD versus brain-first PD. (D) ALFF map for body-first PD versus HCs. (E) ALFF map for brain-first PD versus HCs. (F) ALFF map for body-first PD versus brain-first PD. Warm colors indicate increased values in the former group, and cool colors indicate decreased values. Results were GRF-corrected at cluster-level $P < 0.05$ with voxel-level $P < 0.001$. PD, Parkinson's disease; HC, healthy control.

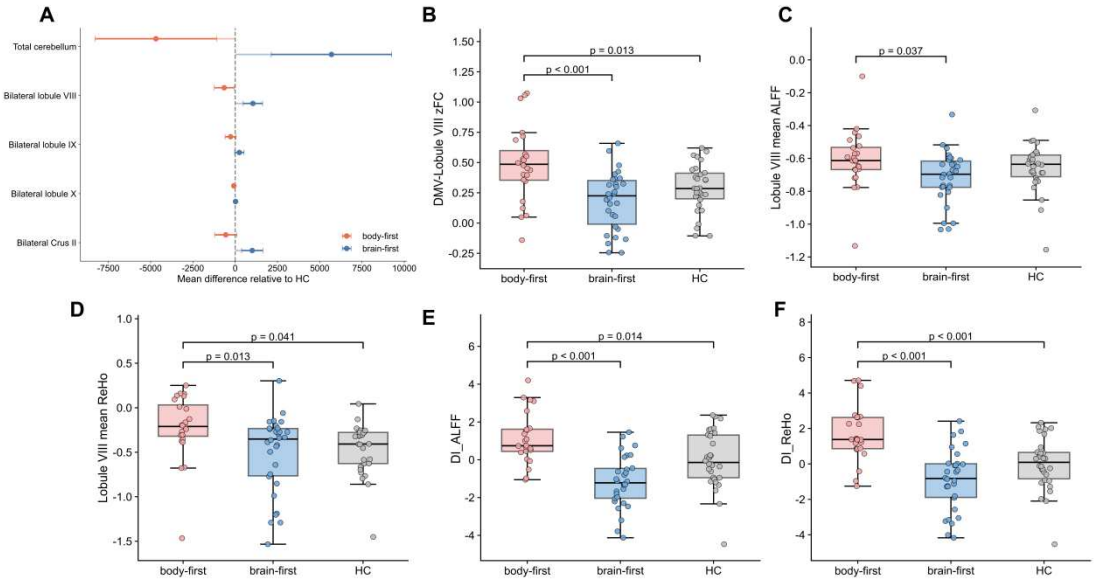


Fig. 3. Cerebellar structure–function convergence. (A) Forest plot showing gray matter volume differences in selected cerebellar regions relative to healthy controls, including total cerebellum, bilateral lobule VIII, bilateral lobule IX, bilateral lobule X, and bilateral Crus II. Positive and negative values indicate higher and lower gray matter volume relative to healthy controls, respectively. (B) DMV–lobule VIII functional connectivity across groups. (C) Mean lobule VIII ALFF across groups. (D) Mean lobule VIII ReHo across groups. (E) ALFF-based decoupling index in bilateral lobule VIII. (F) ReHo-based decoupling index in bilateral lobule VIII. In boxplots, boxes indicate the interquartile range, center lines indicate the median, whiskers indicate the range excluding outliers, and dots represent individual participants. Red, blue, and gray denote body-first PD, brain-first PD, and healthy controls, respectively. DMV, dorsal motor nucleus of the vagus; ALFF, amplitude of low-frequency fluctuation; ReHo, regional homogeneity; HC, healthy control; PD, Parkinson's disease.

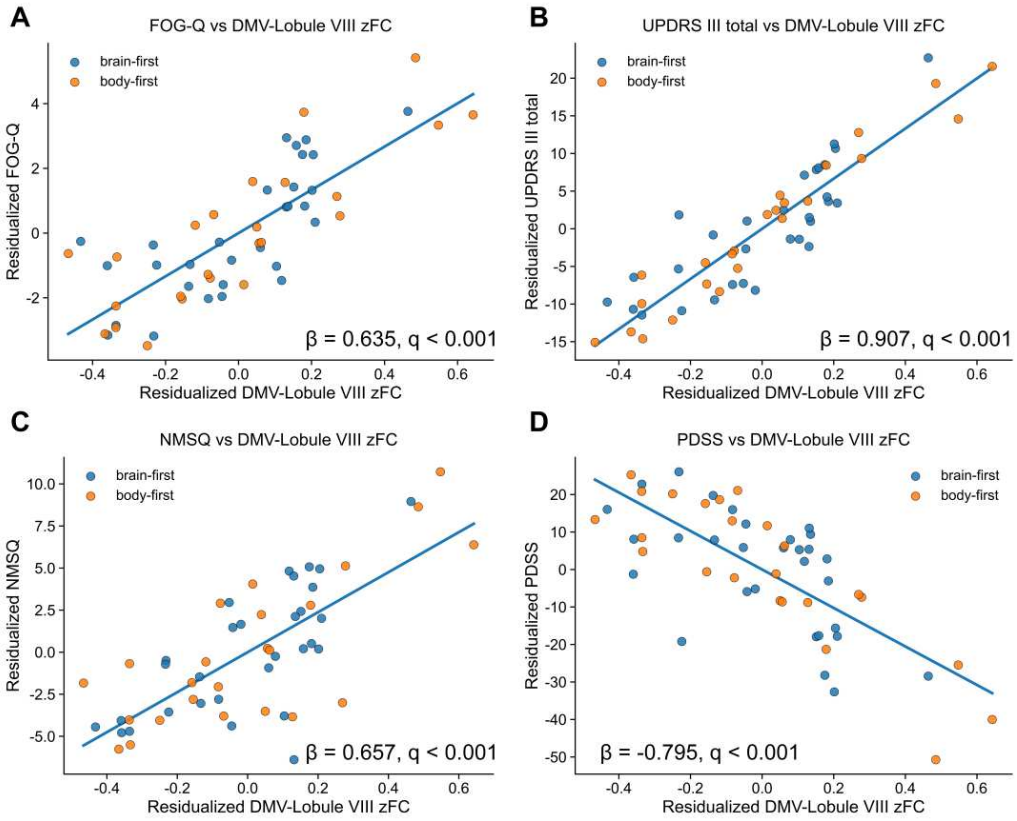


Fig. 4. Adjusted associations between DMV–lobule VIII functional connectivity and clinical burden in PD. Residualized scatter plots show the associations of DMV–lobule VIII functional connectivity with (A) FOG-Q, (B) UPDRS III total, (C) NMSQ, and (D) PDSS in the combined PD cohort. Residual values were derived after adjustment for age, sex, disease duration, levodopa equivalent daily dose, mean framewise displacement, and group. Blue and orange dots indicate brain-first PD and body-first PD, respectively. The fitted line represents the adjusted linear relationship. FOG-Q, Freezing of Gait Questionnaire; UPDRS, Unified Parkinson's Disease Rating Scale; NMSQ, Non-Motor Symptoms Questionnaire; PDSS, Parkinson's Disease Sleep Scale.

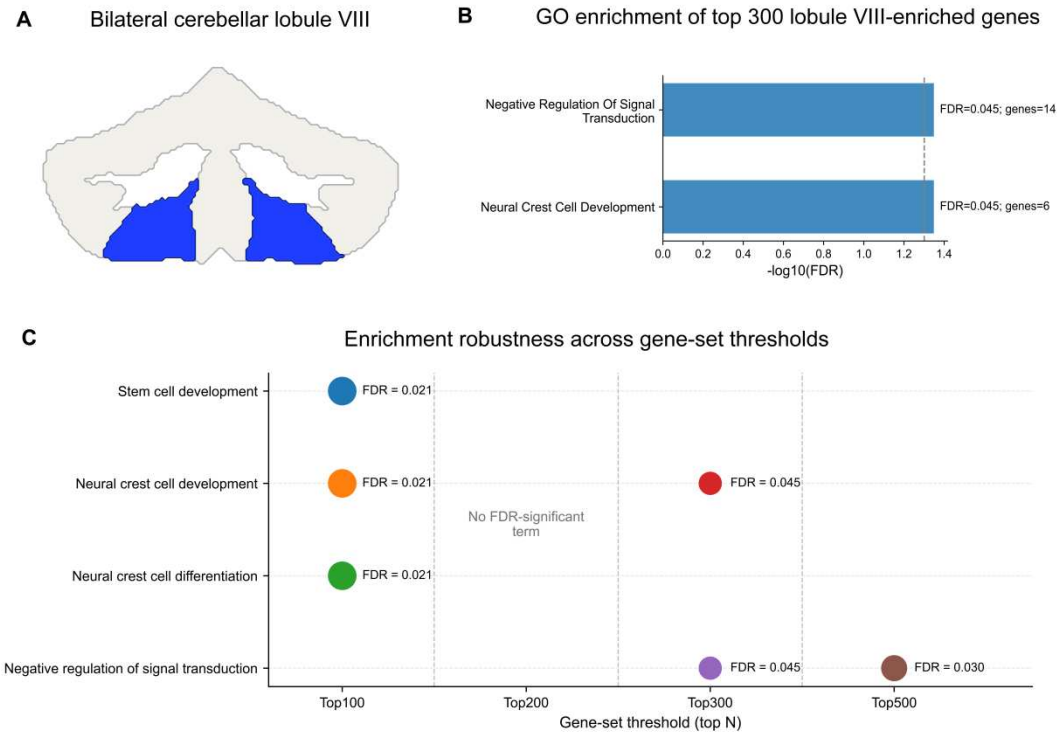


Fig. 5. AHBA-based transcriptomic contextualization of the cerebellar lobule VIII convergence node. (A) Schematic representation of bilateral cerebellar lobule VIII, identified as the multimodal imaging convergence node. (B) GO biological process enrichment of the top 300 lobule VIII-enriched genes. Neural crest cell development and negative regulation of signal transduction were both significantly enriched after FDR correction (FDR = 0.045). (C) Robustness of enrichment findings across the top 100, 200, 300, and 500 lobule VIII-enriched gene sets. Development-related terms were identified at the top 100 threshold, no FDR-significant term was detected at the top 200 threshold, and negative regulation of signal transduction remained significant at the top 500 threshold.

AHBA, Allen Human Brain Atlas; GO, Gene Ontology; FDR, false discovery rate.

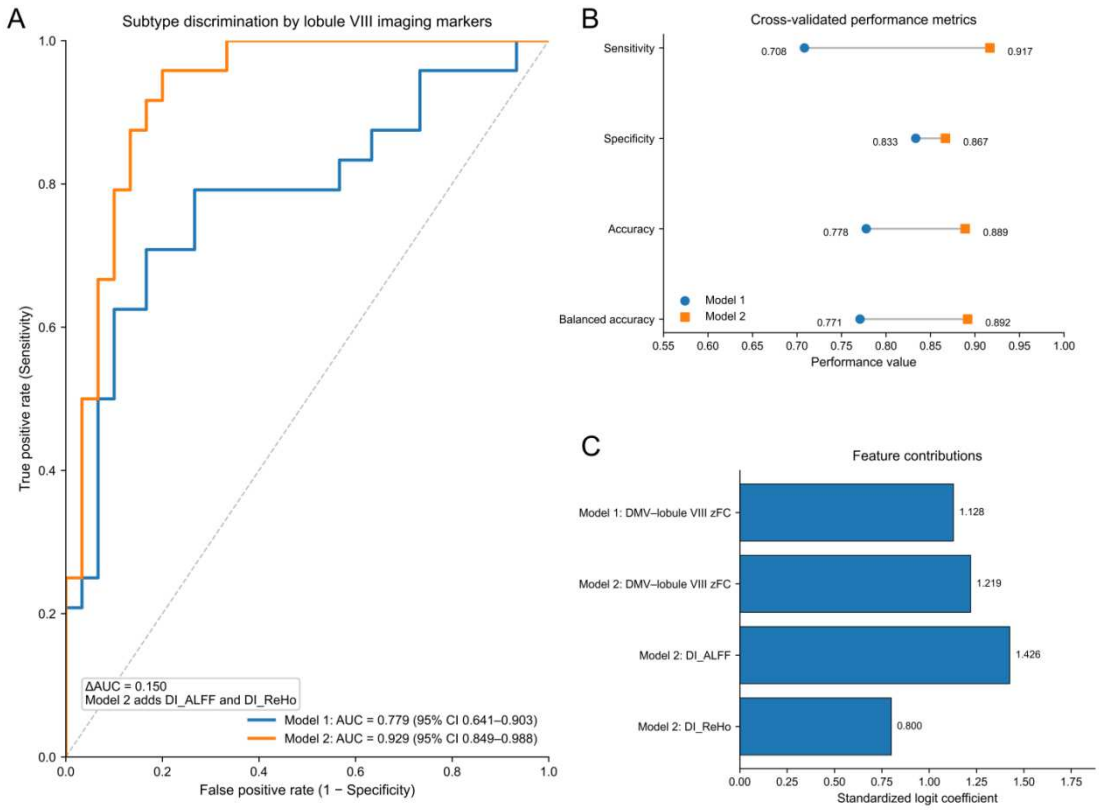


Fig. 6. Exploratory discrimination of body-first and brain-first Parkinson's disease using DMV–lobule VIII imaging markers. (A) ROC curves for Model 1, including DMV–lobule VIII FC alone, and Model 2, combining FC with ALFF- and ReHo-based structure–function decoupling indices. Model 2 showed significantly higher cross-validated discrimination than Model 1, with AUC increasing from 0.779 to 0.929 (ΔAUC = 0.150; paired-bootstrap 95% CI, 0.028–0.279; P = 0.014); the difference was also supported by the DeLong test (P = 0.020). (B) Comparison of cross-validated sensitivity, specificity, accuracy, and balanced accuracy between the two models. (C) Standardized logistic regression coefficients of imaging features included in the classification models. Model performance was evaluated using repeated stratified 5-fold cross-validation. DMV, dorsal motor nucleus of the vagus; FC, functional connectivity; ALFF, amplitude of low-frequency fluctuations; ReHo, regional homogeneity; DI, decoupling index; AUC, area under the curve.

Tables

Table 1. Comparison of demographic and clinical assessments among body-first PD, brain-first PD, and HCs.

	body-first (n=24)	brain-first (n=30)	HCs (n=30)	P values	Post hoc P value		
					body-first vs HCs	brain-first vs HCs	body-first vs brain-first
General information							
Sex (male, N%)	15 (62.50)	18 (60.00)	12 (40.00)	0.2950	NS	NS	NS
Age (years)	64.17 ± 7.68	63.27 ± 10.11	62.73 ± 5.68	0.8089	NS	NS	NS
BMI (kg/m^2)	23.40 ± 2.15	24.26 ± 2.15	23.08 ± 1.25	0.0880	NS	NS	NS
Disease duration (years)	5.37 ± 1.59	5.62 ± 1.60	-	0.5637	-	-	NS
LEDD	611.50 ± 108.00	607.50 ± 117.50	-	0.8991	-	-	NS
Mean FD	0.24 (0.13, 0.45)	0.17 (0.10, 0.25)	0.15 (0.10, 0.26)	0.2815	NS	NS	NS
Assessment scales							
Hoehn & Yahr stage	2.33 ± 0.41	2.17 ± 0.59	-	0.2462	-	-	NS
UPDRS (total)	56.58 ± 17.73	44.63 ± 14.31	-	0.0083	-	-	0.0083
UPDRS I	2.00 (1.00, 5.00)	2.00 (1.00, 3.25)	-	0.2394	-	-	NS
UPDRS II	11.00 (8.00, 18.00)	10.00 (7.00, 13.25)	-	0.3597	-	-	NS
UPDRS III	39.08 ± 11.04	29.73 ± 9.94	-	0.0019	-	-	0.0019
UPDRS IV	1.00 (0.00, 1.00)	1.00 (0.00, 2.00)	-	0.8239	-	-	NS
HAMD	8.67 ± 5.51	6.23 ± 2.91	2.83 ± 2.28	< 0.0001	< 0.0001	0.0017	0.0466
HAMA	6.71 ± 4.73	4.33 ± 2.70	3.80 ± 2.01	0.0039	0.0042	NS	0.0234
NMSQ	12.79 ± 4.74	5.50 ± 3.88	-	< 0.0001	-	-	< 0.0001
PDSS	109.00 (96.50, 115.50)	121.50 (107.00, 130.30)	-	0.0091	-	-	0.0091
RBDSQ	8.33 ± 1.74	7.43 ± 1.33	2.03 ± 1.45	< 0.0001	< 0.0001	< 0.0001	NS
MMSE	26.21 ± 3.87	26.93 ± 2.94	26.80 ± 2.67	0.6794	NS	NS	NS
PDQ39	31.50 (21.50, 64.00)	21.50 (16.00, 43.00)	-	0.1418	-	-	NS

Values are presented as mean ± SD, median (interquartile range), or n (%), as appropriate. Overall group comparisons were performed using chi-square tests, one-way ANOVA, or nonparametric tests, as appropriate, followed by Tukey's post hoc tests for significant omnibus effects.

'-' indicates that no data is available for the HCs.

NS denotes that the corresponding comparison did not reach statistical significance ($P \geq 0.05$).

Supplementary Files

This is a list of supplementary files associated with this preprint. Click to download.

- NEWSupplementarymaterials.docx